Exploring Frequency Domain OCT Systems

John Grasel

Summer 2011

Frequency domain optical coherence tomography allows for in-vivo non-destructive imaging at speeds two orders of magnitude faster than time domain methods while increasing the signal to noise ratio. These benefits are the result of acquiring information on all scatterers in a depth scan all the time. We explore methods of maintaining depth resolution through dispersion compensation and lateral resolution and signal to noise ratio through slab-based OCT and Bessel beams, and we examine methods of resolving the complex conjugate ambiguity. We investigate ISAM and its ability to dynamically refocus data in software, and look at ways of maintaining the phase stability necessary for motion sensitivity. We calculate what specifications a hypothetical instrument would have compared to our current designs.

Contents

1 Introduction

In 2011, it was decided that a new microscope was necessary to meet the HMC OCM lab's biological imaging requirements. The current optical coherence microscopes (OCM), Michelson and Fabry, have wavelengths centered at 1300 nm and 850 nm, respectively. The largest issue with both instruments is their imaging speed. A large 10 million voxel image takes over 10 minutes on the 1300 nm instrument and over 15 minutes on the 850 nm instrument. This is an inconvenience for imaging static objects like cell monolayers, and it is detrimental for images of dynamic objects like frog embryos, where cell motion and cell division during the acquisition blurs the image. While the lateral resolution in the X and Y dimensions is a respectable 5 μm, the axial resolution in the Z direction is 15 μm in air, and 11 μm in water. Improving both the acquisition time and the axial resolution could result in the visualization of cells.

Frequency domain optical coherence tomography (FD-OCT) is a new technology that has the potential to let us achieve the speedup we desire. FD-OCT differs from time domain OCT (TD-OCT) in how the sample image is constructed. In the time domain, coherence gating extracts a voxel at a particular depth in the sample. In the frequency domain method, the interferometric signal created by mixing the sample and reference light is sampled as a function of wavenumber and yields an entire depth scan (A-scan). There are two approaches to FD-OCT: spectral domain OCT (SD-OCT) and swept source OCT (SS-OCT). SD-OCT uses a broad SLD source and a spectrometer in conjunction with a linear camera array as the detector. SS-OCT uses a standard detector, but uses a frequency-swept laser.

2 Design Specifications

2.1 Current Instrumentation

Our current OCM instruments with wavelengths centered at 850nm and 1300nm have lateral resolutions of 5μm, but poor depth resolutions of 15μm in air. Additionally, they take upwards of 5 minutes to image a 10^6-voxel cube (100x100x100) with motion sensitivity enabled. For imaging frog embryos, the movement of the sample during image acquisition and the coarse depth resolution limit our ability to see individual cells. The primary goal of a new instrument is to increase our voxel resolution to 5μm in each direction and acquire a significantly larger $8 \cdot 10^6$-voxel cube (200x200x200) in under a minute.

2.2 Recent Research

FD-OCT is appealing for a new instrument because of its ability to rapidly acquire images. Instead of imaging a single voxel at a time like TD-OCM, FD-OCT images an entire A-scan (axial scan along the depth axis) at once. This enables the microscope to simply scan across the X-Y plane to acquire a three dimensional image. SS-OCT and SD-OCT have been reporting 100 kHz A-scan

rates routinely. A new type of swept source, the Fourier-domain mode-locked (FDML) laser, allows for megaHertz A-scan rates, allowing billions of voxels to be imaged every second. However, because of the tradeoff between speed and image quality,[1] these increases have resulted in decreases in the signal to noise ratio. While many instruments tout their remarkable lateral resolution when imaging the surface of a sample, they ignore the fact that their lateral resolution is reduced by an order of magnitude at the bottom of their image.[2] This image quality may work for some applications, but our group desires an OCT microscope that can achieve uniform, high resolution images throughout a sample, like our current TD-OCM instruments achieve.

2.3 Slab-Based FD-OCT

We have identified a novel design that enjoys the faster acquisition time and SNR benefits of imaging FD-OCT systems while maintaining the uniform high resolution of OCM. Instead of imaging the entire depth of an image with an A-scan, we limit our scan depth, imaging a three dimensional slab by scanning over the X-Y plane. We then move our focus plane down by the depth thickness of our slab and image another slab, repeating until our stacked slabs combine to form a complete image. While the procedure of acquiring multiple slabs increases the image acquisition time, it also increases the SNR and resolution throughout the image. A Slab-Based FD-OCT system can be implemented with either SS-OCT or SD-OCT.

3 Theory

3.1 FD-OCT

Spectral domain and swept source OCT systems share many governing equations. Consider an SD-OCT instrument source with a Gaussian profile with a center wavelength λ_0 and a full-width half-maximum (FWHM) spectral width $\Delta\lambda_{\text{FWHM}}$. The comparable swept source instrument has a center wavelength λ_0 and a FWHM sweep range $\Delta\lambda_{\text{FWHM}}$. In a swept source, we actually sweep over a larger range than $\Delta\lambda_{\text{FWHM}}$ to map out the Gaussian spectra. This sweep range will be called $\Delta\lambda_{\text{sweep}}$. The spectral domain equivalent is the bandwidth of light that the diffraction grating spreads out over the linescan camera elements. In wavenumber space, the center wavenumber becomes

$$k_0 = \frac{2\pi}{\lambda_0} \tag{1}$$

[1] from Equation (39)
[2] from Equation (20)

and the wavenumber change becomes

$$\begin{aligned}\Delta k_{\mathrm{FWHM}} &= 2\pi\left(\frac{1}{\lambda_0 - \Delta\lambda_{\mathrm{FWHM}}/2} - \frac{1}{\lambda_0 + \Delta\lambda_{\mathrm{FWHM}}/2}\right) \\ &= \frac{8\pi\Delta\lambda_{\mathrm{FWHM}}}{4\lambda_0^2 - \Delta\lambda_{\mathrm{FWHM}}^2} \\ &\approx \frac{2\pi\Delta\lambda_{\mathrm{FWHM}}}{\lambda_0^2} \end{aligned} \tag{2}$$

where in the last step we neglect $(\Delta\lambda_{\mathrm{FWHM}})^2$ with respect to λ_0^2. Similarly,

$$\Delta k_{\mathrm{sweep}} \approx \frac{2\pi\Delta\lambda_{\mathrm{sweep}}}{\lambda_0^2} \tag{3}$$

The laser intensity profile $S(k)$, which we'll assume to be a Gaussian, is generally described by its variance σ_k^2 in the equation

$$S(k) = \frac{1}{\sqrt{2\pi\sigma_k^2}} e^{-(k-k_0)^2/2\sigma_k^2} \tag{4}$$

We now wish to take the Fourier transform of this intensity spectrum to find the coherence function $\gamma(z)$.

$$\begin{aligned}\gamma(z) &= \int_{-\infty}^{\infty} S(k) e^{ikz} dk \\ &= \frac{1}{\sqrt{2\pi\sigma_k^2}} \int_{-\infty}^{\infty} e^{-\left(k^2 - 2kk_0 + k_0^2\right)/2\sigma_k^2} e^{ikz} dk \\ &= \frac{1}{\sqrt{2\pi\sigma_k^2}} \int_{-\infty}^{\infty} e^{-\left(k^2 - 2kk_0 + k_0^2 - 2i\sigma_k^2 kz\right)/2\sigma_k^2} dk \\ &= \frac{1}{\sqrt{2\pi\sigma_k^2}} \int_{-\infty}^{\infty} e^{-\left(k - (k_0 + i\sigma_k^2 z)\right)^2/2\sigma_k^2} e^{\left(2ik_0\sigma_k^2 z - \sigma_k^4 z^2\right)/2\sigma_k^2} dk \\ &= e^{-\sigma_k^2 z^2/2} e^{ik_0 z} \end{aligned} \tag{5}$$

where the second term describes the fringes. We notice that we can relate the variance of the coherence function σ_z^2 to the variance of the spectrum σ_k^2 by

$$\sigma_z^2 = \frac{1}{\sigma_k^2} \tag{6}$$

To relate the FWHM spectral width of the source to σ_k^2,

$$S(k_0 + \Delta k_{\mathrm{FWHM}}/2) = S(k_0)/2$$

$$e^{-(\Delta k_{\mathrm{FWHM}}/2)^2/2\sigma_k^2} = e^{-\Delta k_{\mathrm{FWHM}}^2/8\sigma_k^2} = \frac{1}{2}$$

$$\Delta k_{\mathrm{FWHM}}^2 = 8\ln 2 \cdot \sigma_k^2$$

and similarly,

$$\Delta z^2_{\text{FWHM}} = 8 \ln 2 \cdot \sigma_z^2$$

We plug these into Equation (6) to find

$$\Delta z_{\text{FWHM}} = \frac{1}{2} \frac{8 \ln 2}{\Delta k_{\text{FWHM}}} = \frac{4 \ln 2}{\Delta k_{\text{FWHM}}} \tag{7}$$

where the extra factor of one half comes from the transition from optical path length in the interferometer arm, where light passes through the sample twice, to physical depth in the sample. Plugging in Equation (2), we find

$$\Delta z_{\text{FWHM}} = \frac{2 \ln 2}{\pi} \frac{\lambda_0^2}{\Delta \lambda_{\text{FWHM}}} \tag{8}$$

These calculations assumed that the light source was propagating through a material with an index of refraction of 1, like air. In tissue, which we assume due to its water composition has an index of refraction of 4/3, we can say that λ_0 and $\Delta\lambda_{\text{FWHM}}$ are reduced by 3/4, so the axial resolution becomes

$$\Delta z_{\text{FWHM, tissue}} = \frac{3}{4} \Delta z_{\text{FWHM, air}} = \frac{3 \ln 2}{2\pi} \frac{\lambda_0^2}{\Delta \lambda_{\text{FWHM}}} \tag{9}$$

We notice that the axial resolution of the microscope is totally dependent on the spectrum of the source used.

The other parameters of the microscope are governed by the constraints of confocal geometrical optics. The Gaussian beam is focused by a lens with a certain numerical aperture (NA). Numerical aperture is typically defined in optics as

$$\text{NA} = n \frac{D}{2f} \tag{10}$$

where n is the index of refraction of the material surrounding the lens (1 in air), D is the lens diameter, and f is the lens focal length. However, in laser physics, lasers have a Gaussian profile and don't use the full diameter of the lens. Thus, we only care about 86% spot size of the incident beam w_1:

$$\text{NA} = \frac{w_1}{f} \tag{11}$$

where $2w_1$ is the diameter of the beam, measured between the $1/e^2$ intensity points[3] and we assume that $n = 1$. From Gaussian optics, we can relate the spot size w_1 of a laser of wavelength λ_0 at the input of the lens to the minimum (focussed) spot size w_0 at the output:

$$w_0 = \frac{f \lambda_0}{\pi w_1} \tag{12}$$

[3]This could be described as "Full width at e^2 maximum of the intensity"

Combining Equation (13) and Equation (12), we see that

$$\mathrm{NA} = \frac{\lambda_0}{\pi w_0} \tag{13}$$

Solving for the spot size w_0, we see that

$$w_0 = \frac{\lambda_0}{\pi \cdot \mathrm{NA}} \tag{14}$$

which leads to a lateral FWHM (see Equation (18)) of

$$\Delta x_{\mathrm{FWHM}} = \frac{\sqrt{2\ln 2}}{\pi}\frac{\lambda_0}{\mathrm{NA}} \approx 0.375\frac{\lambda_0}{\mathrm{NA}} \tag{15}$$

which we define as the lateral resolution of our system [11]. If we let Δx_{FWHM} become a fundamental quantity of our setup (i.e. a quantity we define from which all others are derived) along with λ_0 and $\Delta\lambda_{\mathrm{FWHM}}$, then Equation (15) determines the numerical aperture of our lens.

3.2 Rayleigh Length

Ideally, the lateral resolution would remain constant throughout the sample. However, the beam is only focused in one depth plane, and it spreads at other depths, dictated by the propagation of intensity of a Gaussian beam. The time-averaged intensity distribution of a Gaussian beam with r as the radial distance from the center axis of the beam and z is the axial distance from the beam's narrowest point (the waist) is

$$I(r,z) = I_0\left(\frac{w_0}{w(z)}\right)^2 \exp\left(\frac{-2r^2}{w^2(z)}\right) \tag{16}$$

where $w(z)$ is the spot size, the radius where the intensity drops off to $1/e^2$ of its axial value, and w_0 is $w(0)$. Looking only at the waist,

$$I(r) = I_0 \exp\left(\frac{-2r^2}{w_0^2}\right) \tag{17}$$

The radius where the intensity drops off to $1/2$ its axial value, $r_{1/2}$ is

$$I(r_{1/2}) = \frac{I_0}{2} \Rightarrow r_{1/2} = w_0\sqrt{\ln 2/2}$$

Thus the lateral full-width-at-half-maximum $\Delta x_{\mathrm{FWHM}} = 2r_{1/2}$ is given by

$$\Delta x_{\mathrm{FWHM}} = w_0\sqrt{2\ln 2} \tag{18}$$

The Rayleigh length (or Rayleigh range) in air, defined as the z coordinate where the beam area has doubled, is given by

$$z_{\mathrm{r}} = \frac{\pi w_0^2}{\lambda_0} = \frac{\pi}{2\ln 2}\frac{\Delta x_{\mathrm{FWHM}}^2}{\lambda_0} \tag{19}$$

In addition, we can then see that, like spot size, our lateral resolution increases as

$$\Delta x_{\mathrm{FWHM}}(z) = \Delta x_{\mathrm{FWHM}} \sqrt{1 + \left(\frac{z}{z_{\mathrm{r}}}\right)^2} \tag{20}$$

Note that in tissue, the effective central wavelength is a factor of 4/3 smaller, so our Rayleigh length becomes 4/3 larger because of Equation (18) and Equation (12).

3.3 Slab-Based FD-OCT

Slab-Based FD-OCT intends to keep Δx_{FWHM} small throughout the scan, so we limit our data acquisition to the slab one Rayleigh length above and below the focus. Thus we want our total imaging length for one slab to be $2z_{\mathrm{r}}$.

Assume that the detector samples data that is linear in wavenumber; this can be done with a k-trigger (only in swept source) or computational re-sampling. Let us define M as the number of samples taken per A-scan. For SS-OCT, the analog to digital converter (ADC) sampling rate f_s on average equal to

$$f_s = f_{\mathrm{sweep}} \cdot M \tag{21}$$

where f_{sweep} is the laser sweep frequency. However, since a swept source's output wavelength is linear in time, a k-trigger would sample nonlinearly in time. We can calculate the minimum and maximum trigger frequencies to be

$$f_{min} \approx f_{\mathrm{sweep}} \cdot M \left(1 - \frac{\Delta\lambda_{\mathrm{sweep}}}{\lambda_0}\right) \tag{22}$$

$$f_{max} \approx f_{\mathrm{sweep}} \cdot M \left(1 + \frac{\Delta\lambda_{\mathrm{sweep}}}{\lambda_0}\right) \tag{23}$$

where we kept terms up to first order in $(\Delta\lambda_{\mathrm{sweep}}/\lambda_0)$ [4]. For SD-OCT, M is equal to the number of pixels we read off of the line scan camera array. Since we have M samples linearly spaced in wavenumber, we can define the wavenumber spacing δk:

$$\delta k = \frac{\Delta k_{\mathrm{sweep}}}{M} = \frac{2\pi}{M} \frac{\Delta\lambda_{\mathrm{sweep}}}{\lambda_0^2} \tag{24}$$

From the Nyquist sampling theorem which arises as an effect of finite sampling, we calculate the distance between measured z data points δz:

$$\delta z = \frac{\pi}{\Delta k_{\mathrm{sweep}}} = \frac{\lambda_0^2}{2\Delta\lambda_{\mathrm{sweep}}} \tag{25}$$

and, completing the circle, the scanning range Δz_{scan},

$$\Delta z_{\mathrm{scan}} = \frac{\pi}{\delta k} = \frac{M\lambda_0^2}{2\Delta\lambda_{\mathrm{sweep}}} = M\delta z \tag{26}$$

[4] For calculation details, see John Grasel's Lab Notebook Pages 132 and 133

Now setting the scanning range Δz_{scan} equal to twice the Rayleigh length in air z_{r}, we calculate the implied M:

$$M = \frac{8\pi}{3\ln 2} \frac{\Delta\lambda_{\text{sweep}} \Delta x_{\text{FWHM}}^2}{\lambda_0^3} \tag{27}$$

With the sources available today, achieving a 5μm lateral resolution results in an M around 10-30, much lower than most OCT systems. Most SD-OCT systems use a line-scan camera array with 1024, 2048, or 4096 pixels (M). Thus, implementing Slab-Based OCT with SD-OCT means wasting the majority of the pixels on an expensive camera. However, with SS-OCT, a small M means we can get away with a slower, cheaper analog to digital converter.

So far, we have assumed that the system has infinite spectral resolution. In the case of SS-OCT, however, our swept source laser has a nonzero instantaneous line-width. For SD-OCT, the spectrometer's pixels have finite size. This finite resolution causes a sensitivity falloff factor as we sample further away from the plane in focus. If we define the spectral width as $\delta\lambda_{\text{FWHM}}$, the distance away from the focus at which the sensitivity is half that of the plane in focus (6 dB) z_{6dB} is [11]

$$z_{\text{6dB}} = \frac{\ln 2}{\pi} \frac{\Delta\lambda_{\text{FWHM}}^2}{\delta\lambda_{\text{FWHM}}} \tag{28}$$

in air.

3.4 Signal to Noise Ratio

In addition, we care about the signal to noise ratio of the system. We'll see the advantage of new FD-OCT systems over TD-OCT.

3.4.1 Frequency-Domain SNR

In addition, we care about the signal to noise ratio of the system. For simplicity, we look at a single reflector located at z_0, we use a single detector, and we only analyze a swept-source system with a rectangular spectral profile[5]. If we examine the signal current i_s over time, if E_R and E_S are the electric fields returning from the sample and reference arms, is equal to

$$i_s(t) = \frac{\eta q}{E} \frac{1}{2} \left\langle |E_R + E_S|^2 \right\rangle \tag{29}$$

where the factor of two reflects the second pass of each field through the beam-splitter and the angular brackets denote integration over the response time of the detector; additionally, η is the quantum efficiency of the detector, q is the electric charge, E is the energy of a single photon, such that the responsivity

[5]The SD-OCT derivation is very similar to the SS-OCT derivation, and it has the same final result. For the dual balanced detection, see Page 213 of [11]

of the detector is the first term of the above equation. If we define P_0 as the average laser power and $k(t)$ is our laser sweep, then our laser's electric field is

$$E(t) = \sqrt{P_0} e^{i(k(t)z - w(t)t)} \tag{30}$$

Defining the reference reflector's position as z_R, and thus the sample position at $z_S = z_R - z_0$, then we find that

$$E_R(t) = \frac{E(t)}{\sqrt{2}} \sqrt{R_R} e^{i2k(t)z_R} \tag{31}$$

and

$$E_S(t) = \frac{E(t)}{\sqrt{2}} \sqrt{R_S} e^{i2k(t)z_S} \tag{32}$$

where the factor of radical two is due to the beamsplitter, and R_R and R_S are the power reflectivities of the reference and sample arms respectively (so their square root is the electric field reflectivities). Combining these with Equation (30) and Equation (29), integrating over temporal angular frequency w since it oscillates much faster than any detector,

$$\begin{aligned} i_s(t) &= \frac{\eta q}{E} \frac{1}{2} \left\langle \left| \sqrt{P_0/2} R_R e^{-wt} + \sqrt{P_0/2} R_S e^{-2iz_0 k(t) - wt} \right|^2 \right\rangle \\ &= \frac{\eta q}{E} \frac{P_0}{4} \left(R_R + R_S + \sqrt{R_R R_S} \left(e^{2iz_0 k(t)} + e^{-2iz_0 k(t)} \right) \right) \\ &= \frac{\eta q}{E} \frac{P_0}{4} \left(R_R + R_S + 2\sqrt{R_R R_S} \cos\left(2z_0 \cdot k\left(t\right)\right) \right) \end{aligned} \tag{33}$$

We take the inverse discrete Fourier transform of $i_s(t)$ to yield $F_s(z)$:

$$F_s(z) = \sum_{m=1}^{M} i_s(t) e^{ik(t)z/M} \tag{34}$$

If we look at the case of equal paths in the sample and reference arms, where $z_0 = 0$, we see that

$$F_s(z_0) = \frac{\eta q}{E} \frac{P_0}{4} \sqrt{R_R R_S} M \tag{35}$$

as the signal power adds coherently. Any other choice of z_0 will give rise to phase factors but will still coherently sum to the same signal peak. The peak signal power is

$$F_s(z_0)^2 = \left(\frac{\eta q}{E} \right)^2 \left(\frac{P_0}{4} \right)^2 R_R R_S M^2 \tag{36}$$

The noise current for shot-noise limited detection is

$$\langle i_n^2(t) \rangle = \frac{\eta q^2}{E} \left(\frac{P_0}{2} \right) R_R \mathrm{BW} = \frac{\eta q^2 f_{\mathrm{sweep}}}{4E} P_0 R_R \tag{37}$$

where in the last step we chose the the detection bandwidth BW as specified by the Nyquist frequency (= $f_s/2$) as defined in Equation (21). Taking the Fourier transforms of i_n yields F_n. By Parseval's theorem,

$$\langle F_n^2 \rangle = M \langle i_n^2 \rangle = \frac{\eta q^2 f_{\text{sweep}}}{4E} P_0 R_R M \tag{38}$$

which scales linearly with M because the noise in each spectral channel is incoherent. We define SNR as follows, substituting in Equation (36) and Equation (38), and setting the sample reflectivity to one:

$$\text{SNR} = \frac{|F_s(z_0)|^2}{\langle F_n^2 \rangle} = \frac{\eta P_0 M}{4E f_{\text{sweep}}} \approx \frac{\eta \lambda_0 P_0 M}{4hc f_{\text{sweep}}} = \frac{2\pi}{3 \ln 2} \frac{\eta}{hc} \frac{P_0 \Delta\lambda_{\text{sweep}} \Delta x_{\text{FWHM}}^2}{\lambda_0^2 f_{\text{sweep}}} \tag{39}$$

where h and c are Planck's constant and the speed of light, respectively. We further define sensitivity in dB as

$$\text{Sensitivity} = 10 \log (\text{SNR}) \tag{40}$$

However, with a Gaussian-shaped source spectrum clipped at $1/e^2$ points, the signal to noise ratio is only 0.598 times as strong.

3.4.2 Time-Domain SNR

The analog of Equation (33) in the time domain is

$$i_{\text{TDOCT}}(z_R) = \frac{\eta q}{E} \frac{P_0}{4} \left(R_R + R_S + 2\sqrt{R_R R_S} e^{-(z_R - z_0)^2 \Delta k_{\text{FWHM}}^2} \cos\left(2(z_R - z_0) \cdot k_0\right) \right) \tag{41}$$

Looking at the third term where the OCT signal resides, we see the peak signal occurs at $z_R = z_0$, where

$$\left\langle i_{\text{TDOCT}}(z_R)^2 \right\rangle = \left(\frac{\eta q}{E} \right)^2 \left(\frac{P_0}{2} \right)^2 \frac{R_R R_S}{2} \tag{42}$$

If we achieve shot-noise limited performance, which is certainly not always the case, then the noise is given by

$$\sigma_{\text{TDOCT}}^2 = 2qIB = 2q \left(\frac{\eta q}{E} \frac{P_0}{2} R_R \right) \left(\frac{1}{\Delta t} \right) \tag{43}$$

where Δt is the integration time suggested by Nyquist sampling of the bandwidth of the detector. The signal to noise ratio is

$$\text{SNR}_{\text{TDOCT}} = \frac{\eta P_0 \Delta t}{2E} \tag{44}$$

Since the integration time for SS-OCT is equal to the inverse of its sweep rate, we calculate that FD-OCT has an $M/2$ improvement in SNR over TD-OCT with a rectangular spectrum. This is a result of the fact that FD-OCT instruments

sample all depths all the time, leading to a potential SNR improvement of M. However, typical OCT methods give rise to complex conjugate ambiguity, leading to the additional factor of one half. Instruments that use direct IQ sampling would have twice the signal to noise ratio; frequency shifting methods have an M that is twice as large.

3.5 Non-Gaussian Spectra

Many swept sources have rectangular spectra, the governing equations of which are slightly different. Let us say that our source has a wavelength center λ_0 and a width of $\Delta\lambda_{\text{rect}}$. We can represent our spectrum $i(k)$ as the difference of two Heaviside functions

$$i(k) = H(k - k_0 + \Delta k_{\text{rect}}/2) - H(k - k_0 - \Delta k_{\text{rect}}/2)$$

the Fourier transform of which is

$$F(z) = \sqrt{\frac{1}{2\pi}}\Delta k_{\text{rect}} e^{ik_0 z}\text{sinc}\left(\frac{\Delta k_{\text{rect}} z}{2}\right)$$

We define the resolution Δz as the width of the main lobe of the function (i.e. until the function reaches 0 at $\pm\pi$). Thus we find that the axial resolution in air is

$$\Delta z = \frac{4\pi}{\Delta k_{\text{rect}}} = \frac{2\lambda_0^2}{\Delta\lambda_{\text{rect}}} \tag{45}$$

which is considerably worse than the resolution given by a Gaussian spectra in Equation (8).

Table 1 summarizes the most important formulas from this section. Three swept sources at different wavelengths, all manufactured by Exalos, are shown for reference.

4 Specific Design Challenges and Solutions

Besides the choice of laser in SS-OCT or source and detector array in SD-OCT, there are other elements of an FD-OCT system that can be added.

4.1 Complex-Conjugate Ambiguity

Recall that our scanning range for a single slab is a Rayleigh length in both directions from the focal plane, with a resulting thickness of $2z_{\text{r}}$. Additionally, the Fourier transform of the fringe data moves it from the wavenumber domain to the position domain with data points at

$$-\Delta z_{\text{scan}}/2,\ -\Delta z_{\text{scan}}/2\ +\ \delta z,\ \ldots\ ,\ \Delta z_{\text{scan}}/2$$

However, a photodetector records a real signal, and the Fourier transform of a real signal in k-space results in a Hermitian signal in position space. This

causes a single reflector located at z relative to the focal plane to appear in two places in our slab, at $-z$ and z, rendering the resulting image useless. This was not a problem in traditional OCT systems, which traditionally have placed the focal plane at the top surface of the sample and discarded the Fourier position data from above the sample. This cuts the scanning range in half, but resolves the ambiguity. However, because we are imaging slabs inside the sample, we cannot set their focal planes at the surface, so we must resolve the ambiguity. Some research has been directed at resolving the ambiguity, which allowed other teams to place their focal planes in the middle of their samples and benefit from increased lateral resolution and SNR. Several methods have been implemented to resolve the ambiguity, but there are two main principles. The first is the use of quadrature interferometry to extract the in-phase and quadrature components of the signal. The second shifts the optical frequency and samples a real signal, and performs hardware or software demodulation.

One of the simplest methods of quadrature interferometry is phase stepping. Typically, five A-scans are imaged serially while incrementing the phase shift by $\pi/2$, time-encoding the real and imaginary components of the signal. The phase shift has been introduced with piezo-electric fiber stretchers and piezo translaters [37, 35]. This method has the downside of requiring several measurements to resolve the ambiguity, a carefully calibrated reference arm, and total phase stability within the system [6]. Similarly, the real and imaginary components can be encoded with different polarization, which has the benefit of being instantaneous but the downside of having a complicated free-space (fibreless) setup and suffering from polarization fading [10].

More recent methods of quadrature interferometry are based on 3x3 fiber couplers. This method on Michelson interferometers using both SS-OCT and SD-OCT [5, 34], a Mach-Zehnder interferometer [12], and unbalanced detection [21, 22]. These designs are simple, but tend to only achieve a conjugate rejection of between 20 and 30 dB due to the difficulty of producing stable quadrature signals.

Another method shifts the peak sensitivity position away from electronic DC, so positive and negative displacements from that position can be discerned unambiguously. Because this technique shifts the complex conjugate, it achieves a complete conjugate rejection (up to the noise floor). As an additional advantage, the DC and autocorrelation artifacts remain centered at DC and can be removed with a high-pass filter. Frequency shifting has been implemented with electro-optic modulators [13] and acousto-optic modulators, but these are expensive, introduce losses into the system, and require hardware demodulation or software post-processing. A recent instrument uses a dispersive optical delay line, which achieves the same benefits but has no sensitivity loss, is low cost, and is easy to implement [9]. The downside to both of these systems is that, because they shift position information to a lower depth, a higher sampling rate is required.

A new technique introduces a dispersion mismatch between sample and ref-

[6] Error can be introduced by interferometer drift between phase-shifted acquisitions

erence arm that can be used to iteratively suppress complex conjugate artifacts and thereby increase the imaging range using a fast dispersion encoded full range (DEFR) algorithm [16, 17, 15]. It achieved a rejection of 55dB on average, but is computationally intensive.

4.2 Bessel Beams

Another technique to extend the depth of focus is the use of Bessel beams instead of Gaussian spherical beams. A conical lens called an axicon forms a Bessel beam in the near field when illuminated with a standard Gaussian spherical beam; it forms a ring in the far field. Unlike a Gaussian beam, whose spot size increases (and thus lateral resolution decreases) away from the focal plane, an ideal Bessel beam's spot size stays constant. This results in constant lateral resolution as a function of depth[20]. Additionally, sensitivity stays constant as well. Bessel beams are self-reconstructing, so opaque obstacles do not create shadows on the image[14]. Finally, to avoid losses resulting from the backscattered beam passing through the axicon twice, a dark-field setup is used, which excludes the unscattered beam from the image and increases image contrast[3]. Bessel beams have been used in both SD-OCT and SS-OCT at A-Scan rates of up to 440kHz [3]. The Bessel beam's intensity as a function of depth z and radial coordinate r is given by

$$I(r,z) = E(R_z)^2 R_z \frac{2\pi k \sin\beta}{\cos^2\beta} J_0^2\left(kr\sin\beta\right) \tag{46}$$

where J_0 is the zero-order Bessel function of the first kind, R_z is the radius of the incident beam that contributes to the intensity at z, E is the energy of the incident beam at that position, and β is an axicon parameter which is determined by the index of refraction of the lens n and the axicon's conical angle α: $\beta = \sin^{-1}\left(n\sin\alpha\right) - \alpha$.

The Bessel beam's advantages arise from greatly extending the exponential falloff of the incident Gaussian beam, since R_z grows much slower than z due to the geometry of an axicon. However, there are many disadvantages that result from the Bessel function in Equation (46). The Bessel function, and thus an ideal Bessel beam, has an infinite number of side lobes. Each of these lobes has a roughly equal amount of power, because the intensity falls off inversely to the radius squared, but area grows as the radius squared [14]. Thus, an ideal Bessel function requires infinite energy; since this is impossible, only approximations are used, which result in actual Bessel beams with finite depth of field and and slightly-varying sensitivity as a function of depth. Even with these approximations, the central lobe of a Bessel field carries around 5% of the power [20] (compared with 86% of a Gaussian beam within a $1/e^2$ radius), and the rest of the power in the side-lobes results in a blurry axial resolution. While the sensitivity is constant, the distribution of power throughout a depth scan reduces the SNR around 20 dB compared to a similar Gaussian system [19]. A dark field detection setup is complex to implement. While the Bessel beam fits many of our design requirements, it introduces many additional problems.

4.3 Gabor-Domain OCT

Another group, headed by Jannick P. Rolland, had similar design considerations and built a SD-OCT system using dynamic focusing [26]. A liquid lens, which changes its focal length on application of an electric field, was used was used to refocus to achieve invariant 3μm resolution throughout a 2mm cube [25]. The microscope used a Gabor Domain OCT (GD-OCT) scheme, an algorithm was used to extract only the in-focus portion of the acquired image, by multiplying the image with a sliding window centered at the microscope's focal plane with a width as the depth of focus. Combining this technique with dynamic focusing allows the extraction of the slabs of the cross section image around each focus position, which are then fused to form an image with nearly invariant resolution [33]. The lens, which only takes 100 ms to focus between slabs, is a small improvement over our actuators. However, its focal positioning is imprecise and must be calculated in software, and it is expensive. The GD-OCT image stitching technique is computationally trivial and can easily be performed in real-time.

4.4 ISAM

Interferometric synthetic aperture microscopy, or ISAM, is a post-processing modality that achieves depth-independent lateral resolution throughout a volume imaged with a fixed focus. ISAM uses similar methods as synthetic aperture radar, or SAR, which combines radar signals from a target illuminated from many directions into a single image. Likewise, ISAM combines all of the A-scans that compose a slab to produce a single image with invariant lateral resolution. The model assumes a scalar model for light propagation that obeys the reduced wave equation [32]. This model is used to propagate a focused beam into the sample and consider the cross-correlation of singlely backscattered photons with the reference pulse. This is used to establish the relationship between the scattering potential and measured signal. ISAM is an inverse scattering procedure to account for these effects [4].

After dispersion compensation, a spacial 2-D Fourier transform is performed over all of the A-scans composing a slab[7]. The data is shifted axially down in wavenumber, and then shifted and diffracted up, compensating for diffraction and moving the focus without net sample movement. A Stolt interpolation maps the wavenumber to axial special frequency, and an inverse 3-D Fourier transform recovers the image [27, 28, 6]. A multiplicative term may be applied to compensate for signal loss away from focus, but there is no way of avoiding the drop in SNR. The benefit of multiple slabs would then be to maintain SNR throughout the image. Also, because data within a slab is combined, the system must have complete phase stability or numerically correct phase disturbances using a cover slip [29]. While this extra processing is complex and takes a lot of time, it is parallelizable and feasible to perform in real-time [31]. In addition,

[7]For more information, see the Projection-Slice Theorem

recent research suggests additional post-processing may reduce autocorrelation artifacts [8].

For a rigorous mathematical overview, see [7]. For details on the algorithm's implementation, see [24]. Additionally, a slightly different adaptation of ISAM was made for high-NA systems (OCM) [30]. The theoretical model was confirmed with experimental evidence [28].

4.5 Dispersion Compensation

Dispersion in the sample or any optical delay line can lead to loss of axial resolution. Dispersion is caused by the group velocity in a medium depending sensitively on the wavelength of light, which is problematic when the source bandwidth is large. Hardware dispersion compensation matches the dispersion in the sample and reference arms by inserting water or glass in the reference arm, but this is ineffective for 3-D imaging because the amount of dispersion in the sample is usually depth-dependent. However, from Parseval's Equality, dispersion does not degrade the power spectrum, so it can be corrected in software without any quality consequences. The Boppart group created a method that minimizes the entropy in the image, which enhances the contrast [23]. This algorithm was extended to FD-OCT by Fujimoto's group [38], but the algorithm is iterative. A non-iterative algorithm uses phase information in the interferogram to calculate a generalized autoconvolution function, but the algorithm only compensates up to second-order [2]. However, this might be sufficient for a FD-OCT setup with a relatively small tuning range. These algorithms appear to be parallelizable, and one has been ported to the GPU [39].

4.6 Phase Stability

Phase stability within a slab is essential for Doppler imaging and ISAM. While a standard Michelson interferometer is immune to phase jumps in the source (with the exception of FDML lasers, which have slow phase drift [1]), it is susceptible to phase changes between the reference and sample arms caused by thermal drift, as well as phase changes between A-scans caused by inconsistent sampling [36]. The solution to the former problem is through a common-path interferometer, a second reference arm that shares a majority of the sample arm's fiber. This adds an additional reflector to the image. If this reflector is positioned to be above the top or below the bottom of the slab, we can slightly increase M to image the calibration reflector. After taking the Fourier transform of each A-scan to move into the position domain, the reflector's phase can be subtracted from each other phase to stabilize the phase between successive A-scans. While this isolates most of the sample arm from thermal drift relative to the reference arm, thermal drift between the calibration arm and the sample head can still cause phase instabilities. Some form of thermal insulation could keep these to a minimum. This solution, known as inserting common path into the instrument, adds relatively little additional complexity to the instrument and the post-processing. Another solution uses a gas-cell as a spectral

reference to increase sensitivity and stability, but the system is complicated to implement[18].

Even with the common path approach, phase instabilities can be introduced from inconsistent sampling. If no k-trigger is used, there is no way of assuring that the linear sampling starts at the same wavelength every time. Even if DAQ is triggered to take M samples every sweep, the precision of when the sampling clock starts cannot be more fine than the internal sample clock rate of the converter. Thus, the phasing of the swept source output and the sample clock drifts ofter time, causing the trigger signal to fall arbitrarily within the sample clock cycle. This results in random shifts of the interferogram in k-space, which by the Fourier Shift Theorem leads to a phase shift in position space. The solution is to force the clocks of the swept source and the analog to digital converter to be perfectly synchronous; using a k-trigger, in addition to reducing other post-processing, realizes this solution.

5 Overall Instrument Design

5.1 Hardware and Data Acquisition

One way in which this is different from our current OCM instruments is that it is more difficult to oversample in the Z direction. While before we specified the Z step size, now our Z step size is determined by Δz_{FWHM}. However, we can oversample by a factor of n if we acquire n slabs spaced $\Delta z_{\mathrm{FWHM}}/n$ from each other.

5.2 Signal Processing

The signal processing steps depend on design decisions such as the method of resolving the complex conjugate ambiguity and the use of a k-trigger in sampling. If the complex signal is directly measured, the first step is to subtract the background DC spectrum. If a k-trigger was not used, the signal must be resampled in linear wavenumber. This is done through interpolating a signal upsampled in the frequency domain, through the use of a forward Fourier transform, zero padding, and an inverse Fourier transform.

Frequency shifting leaves the DC and autocorrelation artifacts centered at DC; since the signal of interest was shifted above DC, these artifacts can be removed with a hardware or software low-pass filter. However, the signal must be demodulated to be centered at DC. First, the Hilbert transform is applied to the signal to remove the conjugate artifact and eliminate aliasing when the signal is shifted to baseband. The shifting is performed through mixing the signal with the negative carrier (modulation) frequency in the time domain, or through the shifting of indices in the frequency domain. Now, since the signal occupies less than half its original bandwidth, it is oversampled by a factor greater than two. Thus, if no k-trigger was used, we need no signal upsampling before the linear wavenumber interpolation. However, if a k-trigger was used,

Figure 1: Diagram of Signal Processing Steps

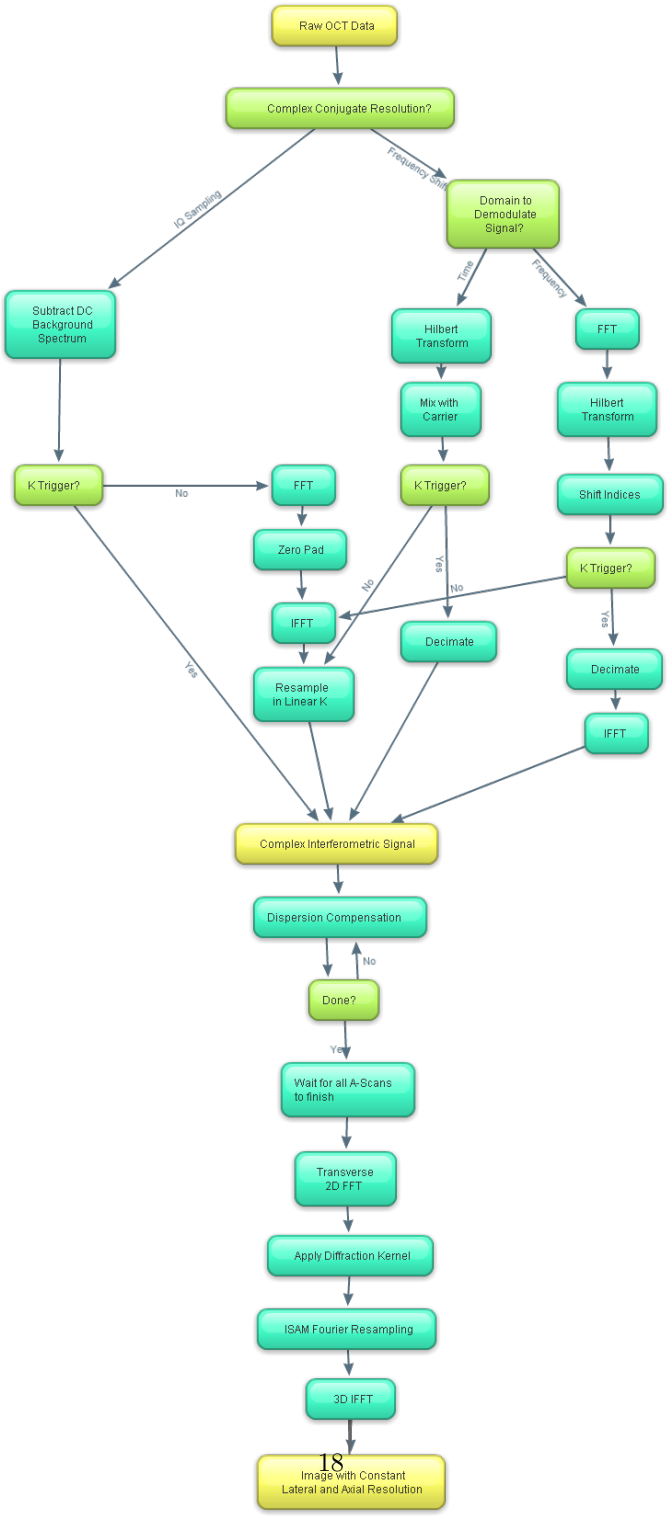

we must reduce the signal's bandwidth through decimation. In the frequency domain, decimation is applied by removing high-frequency components; in the time domain, decimation by a factor of M is a downsampling of the signal by picking out every M^{th} sample.

The result of these steps is a complex interferometric signal sampled at Nyquist in linear wavenumber whose Fourier transform is the axial reflectivity of a the sample at a particular x-y location and depth range.

6 Slab-Based OCT Performance

It is difficult to directly compare FD-OCT systems to TD-OCT systems because the Fourier transform from k-space to position space directly determines Z spacing. Thus, we can no longer specify a 100x100x100 image; instead, we specify that we want 100 X voxels, 100 Y voxels, and a Z scan 500μm long. The scan depth, along with the slab depth thickness (the source's $2z_{\text{r}}$ Rayleigh length), determine the number of slabs and the points per slab, and thus the number of total Z voxels.

While the sweep frequency f_{sweep} is part of what determines the speed of a scan, there are several mechanical factors that limit how quickly data can be acquired. The galvanometers that scan in the XY-plane take roughly 500μs to achieve linear motion, so any data acquired during that time is bad. The actuators take time to move and settle. A safe amount of wait time $W(z)$ in milliseconds where z is the distance to move in μm was empirically determined to be:

$$W(z) = \begin{cases} 3z + 60 & : z \leq 40 \\ 2z + 100 & : z \geq 40 \end{cases}$$

We'll calculate how long each step in the process takes to image N_{slabs} slabs of dimension N_x x N_y. The time taken to acquire a single Z scan t_Z for a slab is

$$t_Z = \frac{1}{f_{\text{sweep}}} \tag{47}$$

so a slab Z-X scan takes

$$t_{ZX} = t_Z N_x \tag{48}$$

If we repeat each Z-X scan X_{scans} times, and we wait for the galvos a time t_{galvo} after every Z-X scan except the last[8], then the time taken to image one slab is

$$t_{ZXY} = t_{ZX} N_y X_{\text{scans}} + t_{\text{galvo}} \left(N_y X_{\text{scans}} - 1 \right) \tag{49}$$

and our total image acquisition time t_{scan} is

$$t_{\text{scan}} = t_{\text{purge}} + t_{ZXY} N_{\text{slabs}} + W(z) \left(N_{\text{slabs}} - 1 \right) \tag{50}$$

where t_{purge} the time we wait at the beginning of every scan to flush the analog to digital converter buffers.

[8] This time sill be absorbed by the actuator wait time

From here, we can generate a table of how long each instrument takes to image various scans. Additionally, we can break down this time and see how long is spent on what task. Table 2 shows how long it takes to acquire a 100x100xZ cube with 500μm depth, compared with a standard 100x100x100 voxel cube in Michelson and Fabry. Despite the fact that we waste over half of the imaging time not collecting data, we still see huge speed improvements over our current instruments. For comparison, Michelson and Fabry waste only 15% of the voxels imaged. However, this small scan size is not making great use of the speed increases of FD-OCT.

If we use a larger scan, acquiring a acquire a 200x200xZ cube with 1000μm depth, we see much more speed improvement. We compare this large scan to a 200x200x200 voxel cube on Michelson and Fabry. The results are shown in Table 3. The 840nm instrument completes this scan in just 21 seconds, well below our goal of one minute. We waste only 30% of our image acquisition time, and over half of that is waiting for the galvos.

7 References

References

[1] Desmond C. Adler, Robert Huber, and James G. Fujimoto, *Phase-sensitive optical coherence tomography at up to 370,000 lines per second using buffered fourier domain mode-locked lasers*, Opt. Lett. **32** (2007), no. 6, 626–628.

[2] Konrad Banaszek, Aleksandr S. Radunsky, and Ian A. Walmsley, *Blind dispersion compensation for optical coherence tomography*, Optics Communications **269** (2007), no. 1, 152 – 155.

[3] Cedric Blatter, Branislav Grajciar, Christoph M. Eigenwillig, Wolfgang Wieser, Benjamin R. Biedermann, Robert Huber, and Rainer A. Leitgeb, *Extended focus high-speed swept source oct with self-reconstructive illumination*, Opt. Express **19** (2011), no. 13, 12141–12155.

[4] P.S. Carney and S.A. Boppart, *Depth of field and resolution meet in new oct approach*, BioOptics World (2011), 19–23.

[5] Michael Choma, Marinko Sarunic, Changhuei Yang, and Joseph Izatt, *Sensitivity advantage of swept source and fourier domain optical coherence tomography*, Opt. Express **11** (2003), no. 18, 2183–2189.

[6] B.J. Davis, T.S. Ralston, D.L. Marks, S.A. Boppart, and P.S. Carney, *Interferometric synthetic aperture microscopy: Physics-based image reconstruction from optical coherence tomography data*, Image Processing, 2007. ICIP 2007. IEEE International Conference on, vol. 4, 16 2007-oct. 19 2007, pp. IV –145 –IV –148.

[7] Brynmor J. Davis, Daniel L. Marks, Tyler S. Ralston, P. Scott Carney, and Stephen A. Boppart, *Interferometric synthetic aperture microscopy: Computed imaging for scanned coherent microscopy*, Sensors **8** (2008), no. 6, 3903–3931.

[8] Brynmor J. Davis, Tyler S. Ralston, Daniel L. Marks, Stephen A. Boppart, and P. Scott Carney, *Autocorrelation artifacts in optical coherence tomography and interferometric synthetic aperture microscopy*, Opt. Lett. **32** (2007), no. 11, 1441–1443.

[9] Al-Hafeez Dhalla and Joseph A. Izatt, *Complete complex conjugate resolved heterodyne swept-source optical coherence tomography using a dispersive optical delay line*, Biomed. Opt. Express **2** (2011), no. 5, 1218–1232.

[10] Zhihua Ding, Yonghua Zhao, Hongwu Ren, J. Nelson, and Zhongping Chen, *Real-time phase-resolved optical coherence tomography and optical doppler tomography*, Opt. Express **10** (2002), no. 5, 236–245.

[11] W. Drexler and J.G. Fujimoto, *Optical coherence tomography: Technology and applications*, Biological and medical physics, biomedical engineering, Springer, 2008.

[12] C Flueraru, H Kumazaki, S Sherif, S Chang, and Y Mao, *Quadrature machzehnder interferometer with application in optical coherence tomography*, Journal of Optics A: Pure and Applied Optics **9** (2007), no. 4, L5.

[13] Erich Götzinger, Michael Pircher, Rainer Leitgeb, and Christoph Hitzenberger, *High speed full range complex spectral domain optical coherence tomography*, Opt. Express **13** (2005), no. 2, 583–594.

[14] R. M. Herman and T. A. Wiggins, *Production and uses of diffractionless beams*, J. Opt. Soc. Am. A **8** (1991), no. 6, 932–942.

[15] Boris Hermann, Bernd Hofer, Christoph Meier, and Wolfgang Drexler, *Spectroscopic measurements with dispersion encoded full range frequency domain optical coherence tomography in single- and multilayered non- scattering phantoms*, Opt. Express **17** (2009), no. 26, 24162–24174.

[16] Bernd Hofer, Boris Považay, Boris Hermann, Angelika Unterhuber, Gerald Matz, and Wolfgang Drexler, *Dispersion encoded full range frequency domain optical coherence tomography*, Opt. Express **17** (2009), no. 1, 7–24.

[17] Bernd Hofer, Boris Považay, Angelika Unterhuber, Ling Wang, Boris Hermann, Sara Rey, Gerald Matz, and Wolfgang Drexler, *Fast dispersion encoded full range optical coherence tomography for retinal imaging at 800 nm and 1060 nm*, Opt. Express **18** (2010), no. 5, 4898–4919.

[18] R.V. Kuranov, A.B. McElroy, N. Kemp, S. Baranov, J. Taber, M.D. Feldman, and T.E. Milner, *Gas-cell referenced swept source phase sensitive optical coherence tomography*, Photonics Technology Letters, IEEE **22** (2010), no. 20, 1524 –1526.

[19] Kye-Sung Lee and Jannick P. Rolland, *Bessel beam spectral-domain high-resolution optical coherence tomography with micro-optic axicon providing extended focusing range*, Opt. Lett. **33** (2008), no. 15, 1696–1698.

[20] R. A. Leitgeb, M. Villiger, A. H. Bachmann, L. Steinmann, and T. Lasser, *Extended focus depth for fourier domain optical coherence microscopy*, Opt. Lett. **31** (2006), no. 16, 2450–2452.

[21] A. Maheshwari, M. A. Choma, and J. A. Izatt, *Heterodyne swept-source optical coherence tomography for complete complex conjugate ambiguity removal*, **5690** (2005), 91–95.

[22] Youxin Mao, Sherif Sherif, Costel Flueraru, and Shoude Chang, *3x3 machzehnder interferometer with unbalanced differential detection for full-range swept-source optical coherence tomography*, Appl. Opt. **47** (2008), no. 12, 2004–2010.

[23] Daniel L. Marks, Amy L. Oldenburg, J. Joshua Reynolds, and Stephen A. Boppart, *Autofocus algorithm for dispersion correction in optical coherence tomography*, Appl. Opt. **42** (2003), no. 16, 3038–3046.

[24] Daniel L. Marks, Tyler S. Ralston, Brynmor J. Davis, P. Scott Carney, and Stephen A. Boppart, *Interferometric synthetic aperture microscopy: tissue structure inferred by computed imaging techniques*, **6864** (2008), no. 1, 686407.

[25] Panomsak Meemon, Supraja Murali, Kye sung Lee, and Jannick P. Rolland, *Gabor domain optical coherence microscopy*, Frontiers in Optics, Optical Society of America, 2008, p. FWW4.

[26] S. Murali, K. S. Lee, and J. P. Rolland, *Invariant resolution dynamic focus ocm based on liquid crystal lens*, Opt. Express **15** (2007), no. 24, 15854–15862.

[27] T. S. Ralston, D. L. Marks, P. Scott Carney, and S. A. Boppart, *Interferometric synthetic aperture microscopy*, Nature Physics **3** (2007), 129–134.

[28] T.S. Ralston, G.L. Charvat, S.G. Adie, B.J. Davis, P.S. Carney, and S.A. Boppart, *Interferometric synthetic aperture microscopy: Microscopic laser radar*, Opt. Photon. News **21** (2010), no. 6, 32–38.

[29] T.S. Ralston, D.L. Marks, P.S. Carney, and S.A. Boppart, *Phase stability technique for inverse scattering in optical coherence tomography*, Biomedical Imaging: Nano to Macro, 2006. 3rd IEEE International Symposium on, april 2006, pp. 578 –581.

[30] Tyler S. Ralston, Daniel L. Marks, Stephen A. Boppart, and P. Scott Carney, *Inverse scattering for high-resolution interferometric microscopy*, Opt. Lett. **31** (2006), no. 24, 3585–3587.

[31] Tyler S. Ralston, Daniel L. Marks, P. S. Carney, and Stephen A. Boppart, *Real-time interferometric synthetic aperture microscopy*, Opt. Express **16** (2008), no. 4, 2555–2569.

[32] Tyler S. Ralston, Daniel L. Marks, P. Scott Carney, and Stephen A. Boppart, *Inverse scattering for optical coherence tomography*, J. Opt. Soc. Am. A **23** (2006), no. 5, 1027–1037.

[33] Jannick P. Rolland, Panomsak Meemon, Supraja Murali, Kevin P. Thompson, and Kye sung Lee, *Gabor-based fusion technique for optical coherence microscopy*, Opt. Express **18** (2010), no. 4, 3632–3642.

[34] Marinko Sarunic, Michael A. Choma, Changhuei Yang, and Joseph A. Izatt, *Instantaneous complex conjugate resolved spectral domain and swept-source oct using 3x3 fiber couplers*, Opt. Express **13** (2005), no. 3, 957–967.

[35] Piotr Targowski, Maciej Wojtkowski, Andrzej Kowalczyk, Tomasz Bajraszewski, Maciej Szkulmowski, and Iwona Gorczynska, *Complex spectral oct in human eye imaging in vivo*, Optics Communications **229** (2004), no. 1-6, 79 – 84.

[36] B. Vakoc, S. Yun, J. de Boer, G. Tearney, and B. Bouma, *Phase-resolved optical frequency domain imaging*, Opt. Express **13** (2005), no. 14, 5483–5493.

[37] M. Wojtkowski, A. Kowalczyk, R. Leitgeb, and A. F. Fercher, *Full range complex spectral optical coherence tomography technique in eye imaging*, Opt. Lett. **27** (2002), no. 16, 1415–1417.

[38] Maciej Wojtkowski, Vivek Srinivasan, Tony Ko, James Fujimoto, Andrzej Kowalczyk, and Jay Duker, *Ultrahigh-resolution, high-speed, fourier domain optical coherence tomography and methods for dispersion compensation*, Opt. Express **12** (2004), no. 11, 2404–2422.

[39] K. Zhang and J.U. Kang, *Real-time numerical dispersion compensation using graphics processing unit for fourier-domain optical coherence tomography*, Electronics Letters **47** (2011), no. 5, 309 –310.

Table 1: **Comparison of Exalos Swept Sources** - The specifications for three swept sources produced by Exalos are shown in the first four rows. The lateral resolution is also defined. From these five parameters, all other aspects of the instrument are determined. Note that the instrument at 1310nm has the highest SNR, the 1050nm has the best resolution, and the 840nm instrument has the longest Rayleigh range. Trade-offs such as these have to be made in the design of an FD-OCT system.

Sources	Formula	1	2	3
Wavelength (nm)	λ_0	1310	1050	840
Wavelength Sweep Range (nm)	$\Delta\lambda_{\text{sweep}}$	100	100	45
Wavelength Sweep FWHM (nm)	$\Delta\lambda_{\text{FWHM}}$	100	100	45
Sweep Rate (kHz)	f_{sweep}	100	100	100
Source Power (mW)	P_0	10	10	5
Lateral Resolution (μm)	Δx_{FWHM}	5	5	5
Axial Resolution (air, μm)	$\Delta z_{\text{FWHM}} = \frac{2\ln 2}{\pi}\frac{\lambda_0^2}{\Delta\lambda_{\text{FWHM}}}$	7.55	4.85	6.90
Axial Resolution (tissue, μm)	$\frac{3}{4}\Delta z_{\text{FWHM}}$	5.66	3.64	5.17
Objective NA	$\text{NA} = 0.37\frac{\lambda_0}{\Delta x_{\text{FWHM}}}$	0.097	0.078	0.062
2x Rayleigh Len (tissue, μm)	$2z_{\text{r}} = \frac{4\pi}{3\ln 2}\frac{\Delta x_{\text{FWHM}}^2}{\lambda_0}$	115.3	143.9	179.9
Samples per A-Scan	$M = \frac{8\pi}{3\ln 2}\frac{\Delta\lambda_{\text{sweep}}\Delta x_{\text{FWHM}}^2}{\lambda_0^3}$	14	27	23
SNR (dB)	$\text{SNR} = \frac{\eta}{4hc}\frac{\lambda_0 P_0 M}{f_{\text{sweep}}}$	122.1	124.0	119.3
Avg ADC Sample Rate (MHz)	$f_s = M f_{\text{sweep}}$	1.40	2.70	2.30
Max ADC Sample Rate (MHz)	$f_{max} = M f_{\text{sweep}}(1 + \frac{\Delta\lambda_{\text{sweep}}}{\lambda_0})$	1.51	2.96	2.42

Table 2: **Time Comparison of Exalos Swept Sources** - Time taken to acquire a 100x100xZ voxel cube with a 500μm scan depth and 6 X-Scans for motion sensitivity.

Exalos Instrument	1310	1050	840
Z Voxels	70	108	69
Scan Time (s)	6.52	5.46	4.32
Speedup Over Michelson	49.7	59.3	75.0
Speedup Over Fabry	72.0	86.0	108.7
% Waste to Purge	10.7%	12.8%	16.2%
% Waste to Galvo	23.0%	21.9%	20.8%
% Waste to Actuator	20.3%	21.3%	21.3%
% Not Wasted	46.0%	43.9%	41.7%

Table 3: **Time Comparison of Exalos Swept Sources** - Time taken to acquire a 200x200xZ voxel cube with a 1000μm scan depth and 6 X-Scans for motion sensitivity.

Exalos Instrument	1310	1050	840
Z Voxels	126	189	138
Scan Time (s)	30.3	24.0	21.0
Speedup Over Michelson	78.6	99.3	113.6
Speedup Over Fabry	116.6	147.3	168.6
% Waste to Purge	2.3%	2.9%	3.3%
% Waste to Galvo	17.8%	17.5%	17.1%
% Waste to Actuator	8.7%	9.7%	10.9%
% Not Wasted	71.2%	69.9%	68.6%